




Quantification of Fault-Zone Plasticity Effects with Spontaneous Rupture Simulations

D. ROTEN,¹  K. B. OLSEN,¹ S. M. DAY,¹ and Y. CUI²

Abstract—Previous studies have shown that plastic yielding in crustal rocks in the fault zone may impose a physical limit to extreme ground motions. We explore the effects of fault-zone non-linearity on peak ground velocities (PGVs) by simulating a suite of surface-rupturing strike-slip earthquakes in a medium governed by Drucker–Prager plasticity using the AWP-ODC finite-difference code. Our simulations cover magnitudes ranging from 6.5 to 8.0, three different rock strength models, and average stress drops of 3.5 and 7.0 MPa, with a maximum frequency of 1 Hz and a minimum shear-wave velocity of 500 m/s. Friction angles and cohesions in our rock models are based on strength criteria which are frequently used for fractured rock masses in civil and mining engineering. For an average stress drop of 3.5 MPa, plastic yielding reduces near-fault PGVs by 15–30% in pre-fractured, low strength rock, but less than 1% in massive, high-quality rock. These reductions are almost insensitive to magnitude. If the stress drop is doubled, plasticity reduces near-fault PGVs by 38–45% and 5–15% in rocks of low and high strength, respectively. Because non-linearity reduces slip rates and static slip near the surface, plasticity acts in addition to, and may partially be emulated by, a shallow velocity-strengthening layer. The effects of plasticity are exacerbated if a fault damage zone with reduced shear-wave velocities and reduced rock strength is present. In the linear case, fault-zone trapped waves result in higher near-surface peak slip rates and ground velocities compared to simulations without a low-velocity zone. These amplifications are balanced out by fault-zone plasticity if rocks in the damage zone exhibit low-to-moderate strength throughout the depth extent of the low-velocity zone (~ 5 km). We also perform dynamic non-linear simulations of a high stress drop (8 MPa) M 7.8 earthquake rupturing the southern San Andreas fault along 250 km from Indio to Lake Hughes. Non-linearity in the fault damage zone and in near-surface deposits would reduce peak ground velocities in the Los Angeles basin by 15–50%, depending on the strength of crustal rocks and shallow sediments. These results show that non-linear effects may be relevant even at long periods, in particular in earthquakes with high stress drop and in the presence of a low-velocity fault damage zone.

Key words: Spontaneous rupture simulation, fault-zone plasticity, non-linear soil behavior.

1. Introduction

Computer simulations of the dynamic rupture process and the resulting wave propagation provide a means to predict near source ground motions which are not sufficiently represented in observed data. In probabilistic seismic hazard assessment, the lack of such observations leads to very high ground motion levels at the low probabilities of exceedance required for critical facilities, such as nuclear installations (e.g., Bommer et al. 2004; Bommer and Abrahamson 2006; Hanks et al. 2005). Physics-based synthetic earthquake ground motion data could complement observations in regions of poor sampling to better constrain ground motion prediction equations (GMPEs). Furthermore, numerical models are able to establish physical limits to ground motions, as exemplified in the case of the proposed Yucca mountain underground repository (e.g., Andrews et al. 2007; Duan and Day 2010; Templeton et al. 2010). These studies have shown that plastic yielding of crustal rocks in the fault damage zone and near the surface limits the maximum peak ground velocities (PGVs) that must be expected at the site.

The absorption of rupture energy by inelastic response of fault-zone material has been the subject of many recent numerical studies on rupture dynamics (e.g., Andrews 2005; Ma 2008; Dunham et al. 2011a; Gabriel et al. 2013). By simulating the M 7.8 ShakeOut earthquake scenario based on a kinematic source parameterization (Graves et al. 2008) in an elasto-plastic medium, the authors found that non-linear material response could reduce long-period (<1 s) PGVs in the Los Angeles basin by 30–70% with respect to visco-elastic solutions (Roten et al. 2014). These findings were somehow surprising, as non-linear effects are typically assumed to be relevant only at higher frequencies (e.g., Field et al.

¹ Department of Geological Sciences, San Diego State University, San Diego, CA, USA. E-mail: droten@mail.sdsu.edu

² San Diego Supercomputer Center, La Jolla, CA, USA.

1998). Because permanent deformations occurred mostly near the fault in these simulations (Roten et al. 2014), the ground motion reductions were mostly attributed to yielding in the fault damage zone, although some deformation was also reported in low-velocity sediments if cohesions were assumed to be near zero. This work aims to systematically explore the reduction of PGVs through fault-zone plasticity by simulating a suite of scenario earthquakes representing a range of magnitudes (6.5, 7.0, 7.5, and 8.0), initial fault stress conditions, and material strength parameters.

Simulations also indicate that low-velocity zones (LVZ), which are encountered around most mature faults, have important effects on dynamic rupture (e.g., Harris and Day 1997; Huang et al. 2014). Because such fault damage zones are typically characterized by lower cohesions and friction angles compared to surrounding wall rock (e.g., Duan and Day 2010), they could potentially also contribute to fault-zone plasticity effects. To quantify the effect of such low-velocity zones on ground motions, we perform a set of dynamic rupture simulations with low-velocity damage zones.

2. Method

We simulate dynamic rupture and wave propagation using the AWP-ODC 3-D finite-difference (FD) code (Olsen 1994; Day and Bradley 2001; Cui et al. 2010) which implements the staggered-grid split-node (SGSN) formulation (Dalguer and Day 2007) for spontaneous rupture. The code includes non-associative Drucker–Prager plasticity (yielding occurs in shear) following the return map algorithm, regularized using time-dependent relaxation (Andrews 2005). In the framework of the SCEC/USGS (Southern California Earthquake Center/US Geological Survey) dynamic earthquake rupture code verification exercise (Harris et al. 2009, 2011), the code has been verified against several other finite-difference and finite-element methods for both visco-elastic (benchmark TPV26) and elasto-plastic (benchmark TPV27) material properties.

For simplicity, we selected a horizontally layered velocity model for most of our dynamic rupture

simulations. The 1D model represents the crustal structure in the Mojave desert in southern California, and has a minimum shear-wave velocity of 500 m/s. To analyze the effects of plasticity for a realistic earthquake rupturing the Southern San Andreas fault, eight of our dynamic rupture simulations were performed for the SCEC community velocity model version 4 (Magistrale et al. 2000). Visco-elasticity was modeled using constant Q (Day and Bradley 2001), which quality factors defined as $Q_s = 50 v_s$ (v_s in km/s) and $Q_p = 2 Q_s$ (e.g., Olsen et al. 2009).

2.1. Initial Stress and Rupture Models

We assume that the shear stress on the fault increases with depth and that the water table is located at the surface. The vertical stress is computed from the lithostatic load and taken as the intermediate principal stress (Dalguer and Mai 2008), σ_2 . We adopt the stress field used by a previous study (Ma 2008; Ma and Andrews 2010), assuming that the major principal stress, σ_1 , is rotated by 45° with respect to the fault and the ratio between effective principal stresses follows $\sigma'_1 = 1.4 \sigma'_2$ and $\sigma'_3 = 0.6 \sigma'_2$. The fault is parallel to the x-axis in our model, with $\tau'_{xy} = 0.4 \tau'_{yy}$ and $\tau'_{xx} = \tau'_{yy} = \tau'_{zz}$.

Because the SGSN FD code is limited to planar, vertical faults, we cannot directly simulate the roughness of the fault which is important for generation of higher frequencies (e.g., Dunham et al. 2011b; Shi and Day 2013). However, effects of fault roughness have been emulated by adding a 2-D random field to the initial shear stress on the fault in previous studies (e.g., Dalguer et al. 2008a; Olsen et al. 2009; Roten et al. 2011; Dalguer and Mai 2012; Baumann and Dalguer 2014). Here, we generally follow the method of Dalguer et al. (2008a) for defining depth-dependent normal and shear stress on the fault, but with a modifications on the emulation of fault roughness. Since the initial stress field must be defined throughout the medium in a non-linear simulation, we prefer to keep the initial stress monotonically increasing with depth and laterally homogeneous. Instead, we emulate fault roughness by applying the random field to the dynamic and static friction coefficient.

Table 1

Fault dimensions (rupture length L and down-dip rupture width W) and von Karman (VK) autocorrelation lengths (along strike, a_x , and along dip, a_z) used for the different magnitude (M) scenario earthquakes

M	6.5	7.0	7.5	8.0
L	25	54	171	541
W	13	17	17	17
a_x	8.0	15.9	31.3	61.7
a_z	3.4	4.90	7.2	10.5

All distances are in kilometers

We use a von Karman autocorrelation function to compute a normalized random field $F(x, z)$, with autocorrelation lengths computed according to established empirical equations (Mai and Beroza 2002) for a strike-slip event of the given magnitude (Table 1), and fault dimensions consistent with recent earthquake fault scaling relations (Leonard 2010). We use a Hurst coefficient of 0.75 (Baumann and Dalguer 2014). Dynamic rupture is simulated using a linear slip-weakening law. The critical slip distance D_{\max} was set to 0.3 m. For rupture model A, the average friction coefficient, $\bar{\mu}_d$, is taken as 0.35, and the average static friction coefficient $\bar{\mu}_s$ is assumed to be 0.5. This results in an average stress drop of about 3.5 MPa. For rupture model B, we use $\bar{\mu}_d = 0.30$ and $\bar{\mu}_s = 0.6$, which doubles the average stress drop. The static friction coefficient at position (x, z) on the fault is perturbed using the random field, such that it is always above or equal to the ratio between the initial shear and normal stress at that position (Fig. 1):

$$\mu_s(x, z) = \bar{\mu}_s - \left(\bar{\mu}_s - \frac{\tau'_{xy}(x, z)}{\tau'_{yy}(x, z)} \right) F(x, z). \quad (1)$$

The dynamic friction coefficient is then calculated by adjusting the average value with the same amount:

$$\mu_d(x, z) = \bar{\mu}_d + (\mu_s(x, z) - \bar{\mu}_s). \quad (2)$$

The dynamic failure stress may be above the initial shear stress (Fig. 1a), representative of dynamic overshoot during past earthquakes. The initial stresses for rupture model B were generated using the same realizations of the random field as rupture model A. However, due to the higher stress drop in rupture model B, we reduced the fault dimensions to obtain the target scenario magnitudes. To avoid

abrupt termination of the rupture at the fault boundaries, the dynamic friction coefficient is linearly increased to the value of μ_s inside a transition zone at the edges and the bottom of the fault (Fig. 1b). Outside of the fault, we use $\mu_s = \mu_d = 10^5$. Fault cohesion is tapered from 1 MPa at the surface to zero below 3 km depth using a ramp function. The stress drop generally increases with depth, but can assume negative values (Fig. 1c). The rupture is started by prescribing a smooth forced rupture within the nucleation patch, with the forced rupture velocity decreasing with distance from the hypocenter (Bizzarri 2010; Barall 2010).

2.2. Models of Rock-Mass Strength

In our implementation, the Drucker–Prager yield stress $Y(\tau)$ is expressed in terms of cohesion c and friction angle φ ,

$$Y(\tau) = \max(0, c \cos \varphi - (\tau_m + P_f) \sin \varphi) \quad (3)$$

where τ_m is the mean stress and P_f the fluid pressure. Both cohesions and friction angles may be determined in the laboratory from small samples, such as drill cores. However, in a jointed rock mass, the strength tends to decrease with increasing sample size, as a larger sample is more likely to contain pre-existing fractures on which failure will occur (e.g., Wyllie and Mah 2004). Civil and mining engineering problems often use the generalized Hoek–Brown failure criterion, which accounts for the reduction of shear strength by the presence of joints in the rock.

The Hoek–Brown criterion describes the strength of intact rock with the unconfined compressive strength σ_{ci} and the material constant m_i , which is provided in tables for various rock types. Typical values are $m_i \approx 7$ for weak sedimentary rocks, such as shales or siltstones, $m_i \approx 17$ for stronger sedimentary rocks like sandstone or greywackes, and $m_i \approx 25$ for strong igneous or metamorphic rocks, such as granite, diorite, or gneiss. The reduced value m_b is evaluated from the material constant m_i using the Geological Strength Index (GSI) of the rock. The value of the GSI ranges from 0 to 100 to reflect different geologic conditions, related to the degree of fracturing and weathering. A GSI above 80 indicates intact, undisturbed rock; a GSI of 50 reflects a blocky

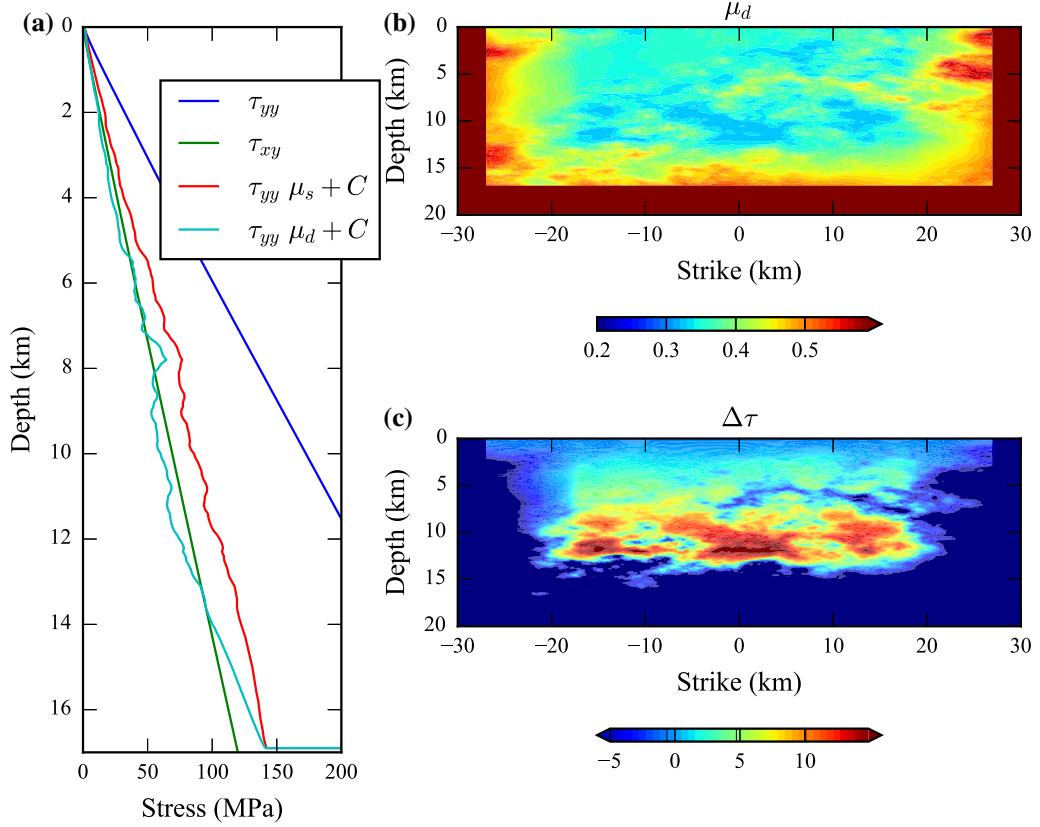


Figure 1

Initial stress for an $M7$ scenario earthquake in rupture model F. **a** Normal stress τ_{yy} , shear stress τ_{xy} , and static and dynamic frictional strength as a function of depth at the epicenter location. **b** Dynamic friction coefficient μ_d and **c** stress drop $\Delta\tau$ on the fault

and disturbed rock, while a GSI value of 30 represents a disintegrated, heavily broken or tectonically deformed rock mass.

The Hoek–Brown model (Hoek et al. 2002) also provides empirical equations to approximate the curved Hoek–Brown failure envelope using a linear Mohr–Coulomb failure line. Equivalent friction angles and cohesions derived in this way allow the application of the Hoek–Brown criterion in numerical models that incorporate Mohr–Coulomb or Drucker–Prager yield conditions.

To cover a wide range of possible rock-mass strengths, we define equivalent cohesions and friction angles using three different sets of Hoek–Brown parameters (Table 2). The granite model represents a very good quality hard rock mass, with $\text{GSI} = 75$, $m_i = 25$, and $\sigma_{ci} = 1.5 \times 10^8$ Pa. The sandstone model is an average quality rock mass with $m_i = 17$

and $\text{GSI} = 50$, while the shale model represents a poor quality rock mass with $m_i = 7$ and $\text{GSI} = 30$. In the sandstone and shale models, we increase σ_{ci} with depth, as the initial stress would otherwise exceed the strength of the rock mass at depths greater than a few km. For the shale, we predict the unconfined compressive strength (MPa) from the P-wave velocity v_p (km/s) based on a published empirical equation (Horsrud 2001):

$$\sigma_{ci} = 0.77 v_p^{2.93}. \quad (4)$$

A similar empirical equation is used for the sandstone model (Chang et al. 2006), where

$$\sigma_{ci} = 1.4138 \times 10^7 \Delta t^{-3}, \quad (5)$$

with the interval time Δt (inverse P-wave velocity) specified in $\mu\text{s}/\text{ft}$. In the absence of strong tectonic disturbance (i.e., in the absence of a low-velocity

Table 2

Hoek–Brown parameter, m_i , geological strength index GSI at the surface, and unconfined compressive strength σ_{ci} in the three models of rock-mass strength

Name quality	Shale poor	Sandstone average	Granite good
m_i	7	17	25
GSI	30	50	75
σ_{ci}	Eq. 4	Eq. 5	1.5×10^8 Pa

fault damage zone), the rock-mass behavior approaches that of intact rock at depths of about 1 km or more, where the GSI value approaches 100 (Marinos et al. 2005). In our rock strength models, we account for the tightening of the rock-mass structure with depth by linearly increasing the GSI from its surficial value (Table 2) to 100 at a depth of 1 km. Figure 2 shows the equivalent friction angle φ , equivalent cohesion c , and resulting rock strength $Y(\tau)$ (Eq. 3) in our three rock strength models as a function of depth. Due to the non-linearity of the Hoek–Brown failure envelope, equivalent friction angles decrease with increasing stress, while equivalent cohesions increase. Without an LVZ, yield stresses are quite similar for the three rock strength models at depths greater than 1 km (Fig. 2c).

2.3. Definition of Fault Damage Zone

Observations of fault-zone trapped waves suggest that shear-wave velocities are 30–50% lower within a 100–400 m-wide low-velocity zone (LVZ) around the fault than in surrounding wall rock (e.g., Vidale and Li 2003; Li et al. 2004; Cochran et al. 2009). For our simulations, we adopted the simplified fault-zone representation defined by Graves and Pitarka (2016). Shear-wave velocities are reduced by 30% (relative to wall rock) within a 450 m-wide inner fault zone. Inside the outer fault zone, at distances between 225 and 750 m from the fault, shear-wave velocities increase linearly from the inner zone value to the wall rock level. The inner fault zone extends to a depth of 4 km, while the outer fault zone reaches 6 km, and a linear taper is also applied in the vertical direction between 4 and 6 km depth. Figure 3a shows the shear-wave velocity within the fault zone. In our model, P-wave velocities and densities in the damage

zone are left unchanged. As the shear and normal stresses on the fault remain the same as in the simulations without LVZ, the only change required in the source definition concerns the forced rupture velocity, defined as 70% of the shear-wave velocity.

For the non-linear simulations, we assume that the rocks inside the LVZ are no longer intact, even at depths exceeding 1 km. Inside the inner LVZ, at distances of less than 225 m from the fault and at depths of less than 4 km, we assign a GSI equal to the surface value (i.e., 30 for the shale, 50 for the sandstone, and 75 for the granite model). In the outer damage zone, the GSI gradually changes from the inner zone level to the wall rock value, using the same taper as for the shear-wave velocities. Outside the outer LVZ, the GSI reaches 100 at depths above 1 km. Figure 3b shows the GSI in the LVZ for the sandstone model. The lower GSI in the LVZ results in lower equivalent friction angles (Fig. 2a) and equivalent cohesions (Fig. 2b) than outside the LVZ. Yield stresses inside the LVZ (Fig. 2d) are sensitive to the choice of Hoek–Brown parameters, and close to the initial stress in the shale model.

3. Ground Motions from Layered Structure Models

In the layered structure models, dynamic rupture was simulated for four different magnitudes (6.5, 7.0, 7.5, and 8.0), and two rupture models (A and B) were tested for each scenario earthquake magnitude. For each magnitude and rupture model combination, the simulation was carried out for a linear (visco-elastic) medium and a non-linear (visco-plastic) medium using the shale, sandstone, and granite rock strength models.

3.1. Reduction of Average Near-Fault Ground Motions

Figure 4 shows the final slip and peak slip rates obtained during a representative simulation, using rupture model A for an $M 7$ scenario event without an LVZ. A maximum slip of up to 3.3 m is obtained on the fault, with up to 2.2 m reaching the surface (Fig. 4a). Allowing for plastic yielding does not

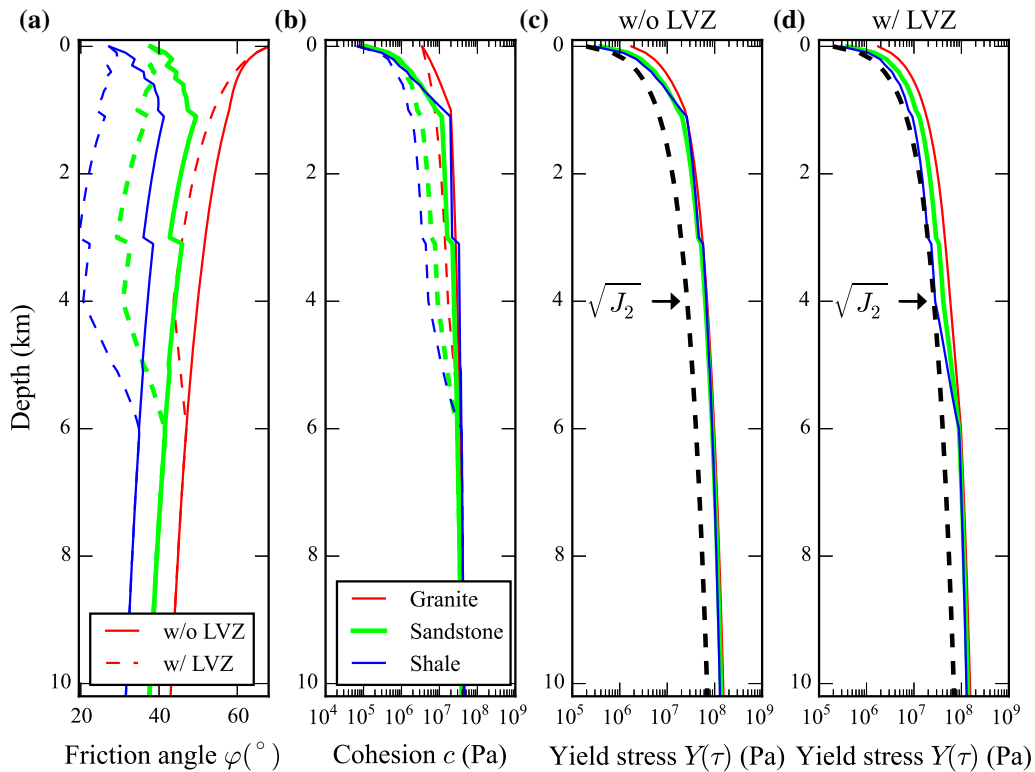


Figure 2

a Equivalent friction angle φ and **b** equivalent cohesion c derived from Hoek–Brown parameters in our rock strength models without (*solid*) and with (*dashed*) low-velocity zone (LVZ). **c** Yield stress $Y(\tau)$ without LVZ and **d** with LVZ. The *black dashed line* in **c** and **d** shows $\sqrt{J_2}$ for the initial stress in our simulations

significantly alter the final slip on the fault (Fig. 4b), except in the uppermost 500 m (Fig. 4c). Plastic yielding reduces the average surface slip from 1.6 to 0.35 m for the shale and 0.57 m for the sandstone model. In the case of the granite, no reduction of surface slip is observed.

In the linear simulation, high peak slip rates (PSR > 3 m/s) occur close to the free surface in the left portion of the fault (Fig. 4d). These high near-surface PSRs are reduced to less than 2 m/s in the non-linear simulation for the shale model (Fig. 4e). Average surface PSRs exceed 2 m/s in the linear case, but are reduced to less than 1 m/s in the non-linear case using the shale and sandstone models (Fig. 4f). The reduction in average PSR is less pronounced for the granite model.

Figure 5a–d compares average ground motions across the fault for the different scenario magnitudes and material types using rupture model A. Average

near-fault PGVs increase with magnitude, although near-fault PGVs in the $M 7$ scenario are comparable to the $M 7.5$ scenario due to the patch of high near-surface PSRs (Fig. 4d). In rupture model A, non-linearity only affects average ground motions within a narrow zone of less than ~ 2 km around the fault. In the simulations for the shale and sandstone model, PGVs exhibit a trough on top of the fault, with the highest values occurring 300–500 m from the surface rupture. With respect to the linear simulation, PGVs near the surface rupture are reduced by up to 30% for the shale, up to 20% for the sandstone, but less than 3% for the granite (Table 3). Surprisingly, these reductions are not exhibiting a clear dependency with respect to the scenario earthquake magnitude, at least not within the small number of source realizations presented in this study.

Because rupture model B is characterized by a higher stress drop, it yields much higher average

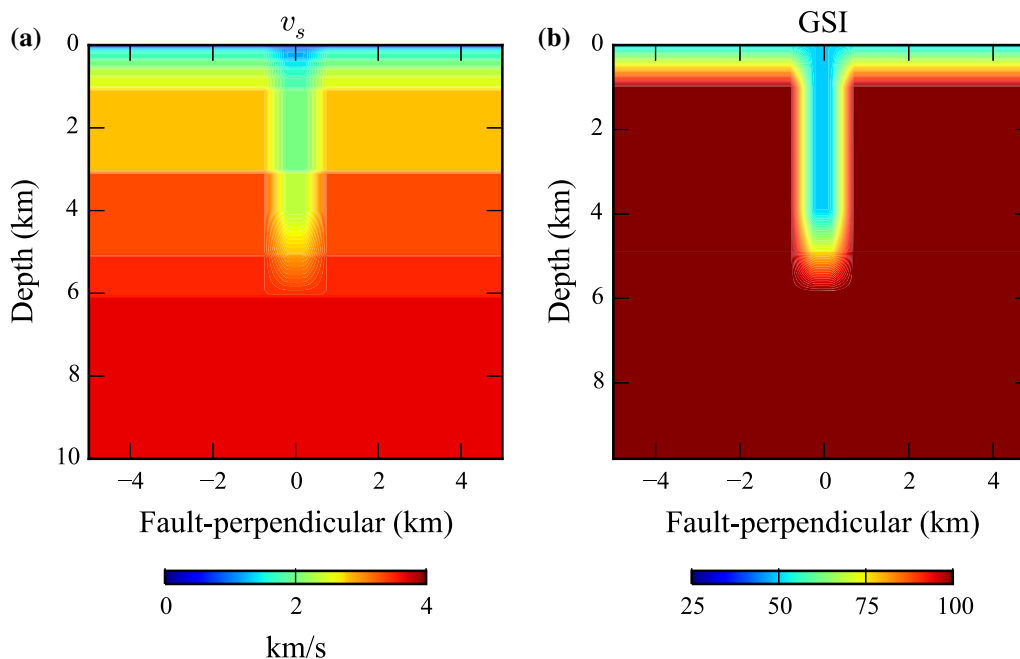


Figure 3

Cross section of fault damage zone showing (a) shear-wave velocity v_s and (b) geological strength index GSI for sandstone model

PGVs than rupture model A (Fig. 5e–h). Furthermore, plastic yielding has a much higher effect on average ground motions in rupture model B compared to rupture model A (Fig. 5e–h). Within 100 m of the fault, average PGVs are reduced by 34–43% in the shale, 27–35% in the sandstone, and up to 15% in the granite with respect to the linear simulation (Table 3). Compared to rupture model A, plasticity reduces PGVs inside a much wider zone around the fault (Fig. 5).

3.2. Reduction of Ground Motion Extremes

To analyze the impact of non-linearity on ground motion extremes, we computed the cumulative distribution of PGVs inside a zone extending 5 km in both fault-perpendicular directions of the rupture (Fig. 6).

Plastic yielding in the fault zone tends to reduce the occurrence and severity of extreme ground motions. As already noted for mean PGVs, the importance of non-linearity is less pronounced for the average stress drop scenarios (Fig. 6a–d) than for the high stress drop scenarios (Fig. 6e, f). In the low

stress drop scenarios, no significant reduction of extreme PGVs takes place in the granite except for the M 8.0 scenario (Fig. 6d), where the highest PGVs are reduced from 4.4 to 4.0 m/s. Even for the shale and sandstone models, non-linearity reduces PGVs significantly only for the M 7.0 and M 8.0 average stress drop scenarios (Fig. 6b, d, respectively). In the high stress drop scenarios, on the other hand, non-linearity reduces PGV extremes by up to 50%. The most dramatic effect is seen in the M 8.0 high stress drop scenario (Fig. 6h), where PGVs are reduced from more than 9 m/s to 7 m/s for granite, and to less than 4.5 m/s for shale. These reductions are comparable to those reported for the Yucca mountain simulations (e.g., Andrews et al. 2007; Duan and Day 2010).

Both linear and non-linear simulations suggest that the PGV at a given frequency of occurrence increases with increasing magnitude, although the rate of increase is slowed down in the non-linear simulations. For example, PGVs at an occurrence of 10^{-4} increase from 4.2 to 9.2 m/s between the M 7.5 and M 8.0 high stress drop scenarios in the linear case, while they increase only from 3.3 to 4.4 m/s in

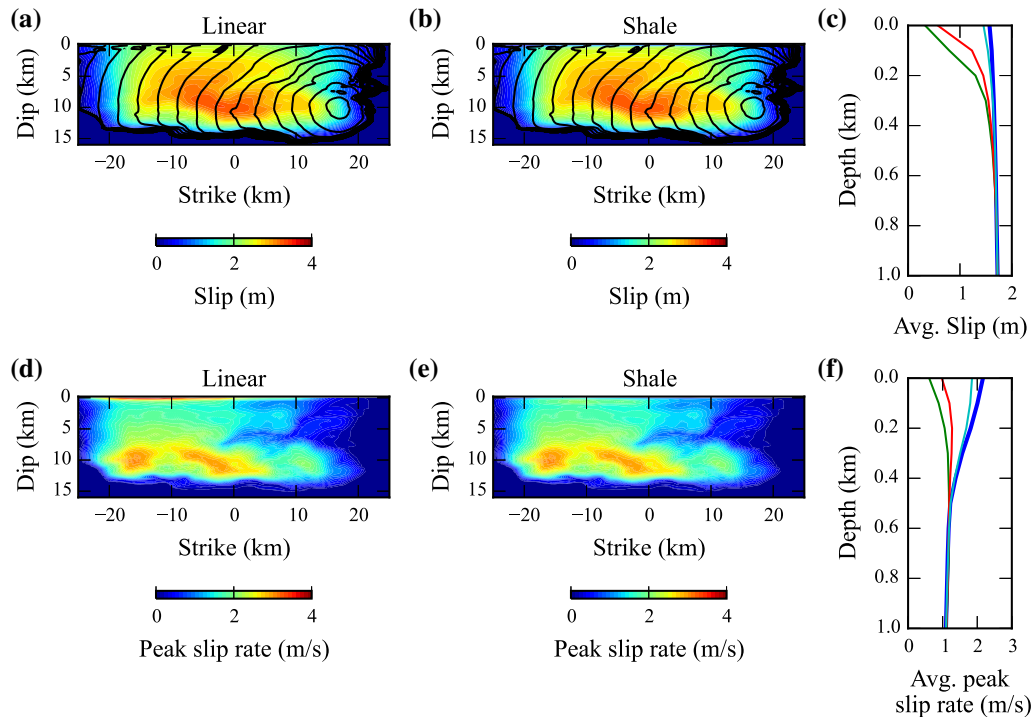


Figure 4

Final slip and peak slip rates obtained for the M 7.0 scenario earthquake based on rupture model A. **a** Final slip and rupture times (1 s contours) for a linear (visco-elastic) simulation and **b** a non-linear (elasto-plastic) simulation using the shale rock strength model. **c** Average final slip as a function of depth in the top km obtained for the linear case (*blue*), granite (*cyan*), sandstone (*red*), and shale (*green*). **d** Peak slip rates for linear case and **e** non-linear case using shale model. **f** Avg. peak slip rates in the top kilometer. *Colors* as in **c**

the non-linear case for the shale (Fig. 6g, h). More simulations, with different realizations of random stress drop distributions, will need to be carried out to establish whether a saturation of ground motions takes place above a certain magnitude.

4. Effect of Low-Velocity Zone (LVZ) on Ground Motions

Dynamic rupture simulations for rupture model A were repeated for a fault surrounded by an LVZ for all four magnitudes.

4.1. Reduction of Near-Surface Slip and Slip Rates

In the linear case, the LVZ promotes higher peak slip rates within the shallow part of the crust. Figure 7 illustrates this observation for the case of the M 7.5

scenario, with slip rates exceeding 3 m/s in the upper left corner of the fault if the LVZ is present (Fig. 7c). As noted earlier, these high peak slip rates are damped out by non-linearity in the shallow part of the fault (Fig. 7c).

In the linear case, the LVZ has a little impact on the final slip reaching the surface, which a mean surface slip of 2.5 m in the M 7.5 scenario (Fig. 8). Plastic yielding results in a shallow slip deficit (SSD), which is more pronounced, and more sensitive to rock strength, if an LVZ is present. Without LVZ, plasticity reduces slip only in the upper 500 m in the shale and sandstone models (Fig. 8a). In the presence of an LVZ, the depth extent of the SSD reaches ~ 1 km in the sandstone and ~ 4.5 km in the shale model (Fig. 8b). In the granite model, surface slip is almost identical to the linear case, and no SSD is observed with or without the LVZ. We note that the granite model, representing intact, very good quality rock, would not be a realistic representation of a fault

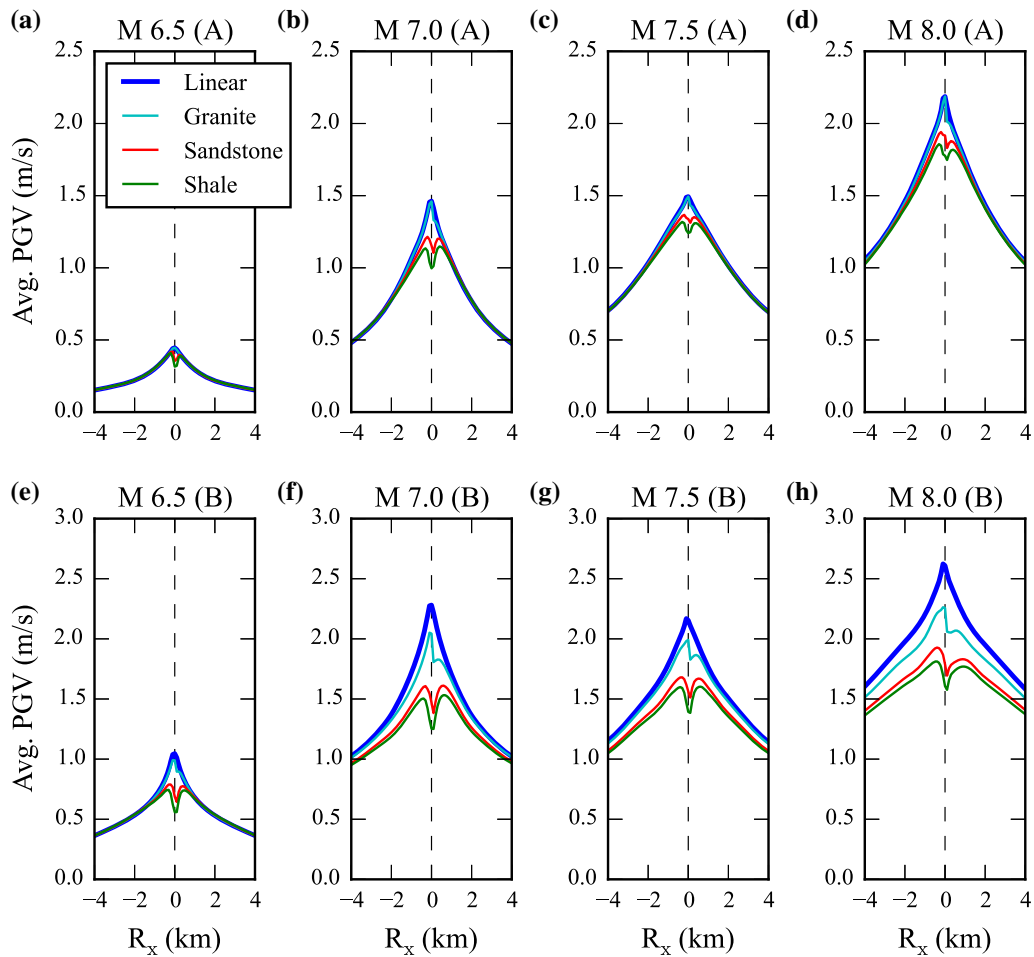


Figure 5

Average horizontal PGVs (defined as the maximum of the horizontal, 2-D velocity vector) across the fault for the four different scenario magnitudes and rupture models A and B. The *dashed line* shows the location of the fault

damage zone where fracturing has led to a significant reduction in shear-wave velocities. It is only shown to illustrate the sensitivity of the simulation results to rock strength parameters.

In contrast to the final slip, peak slip rates reach a maximum close to the surface. Without an LVZ, surface PSRs average to 1.9 m/s for the $M 7.5$ scenario (rupture model A) in the linear case (Fig. 8c). Plasticity reduces mean PSRs to less than 1 m/s in the shale model (Fig. 8c), in line with results seen for the $M 7.0$ scenario (Fig. 4f). If an LVZ is present, linear PSRs increase to an average of 3 m/s near the surface (Fig. 8d). In the shale and sandstone models, fault-zone plasticity brings these high PSRs back down to ~ 0.5 and ~ 1.5 m/s, respectively.

These results indicate that trapping effects caused by the impedance contrast between the LVZ and wall-rock are, at least partly, offset by increased non-linear attenuation in the fractured rock of the fault damage zone. In the final slip and peak slip rates for the shale, an inversion occurs at ~ 3 km depth, which reflects a shallow patch of reduced slip in this model.

The distribution of accumulated plastic strain across the fault zone (Fig. 9) supports this interpretation. Without LVZ, widespread damage occurs only at depths of less than ~ 1 km; at greater depth, damage is localized and observed only on the fault itself. As already noted by Ma (2008), the width of the flower-like damage zone increases with decreasing rock strength. If the LVZ zone is included, off-fault

Table 3

Reduction of peak ground velocities (PGVs) with respect to the linear case within 100 m of the fault obtained using the different models of rock strength, scenario magnitudes, and rupture models

Source	Description	Material	M 6.5 (%)	M 7.0 (%)	M 7.5 (%)	M 8.0 (%)
A	$\bar{\mu}_s = 0.35$	Shale (weak)	25	30	16	18
	$\bar{\mu}_d = 0.50$	Sandstone (moderate)	14	20	10	13
	$\Delta\tau \approx 3.5$ MPa	Granite (strong)	0	2	1	2
B	$\bar{\mu}_s = 0.30$	Shale (weak)	43	44	34	37
	$\bar{\mu}_d = 0.60$	Sandstone (moderate)	32	36	27	31
	$\Delta\tau \approx 7.0$ MPa	Granite (strong)	7	13	10	15

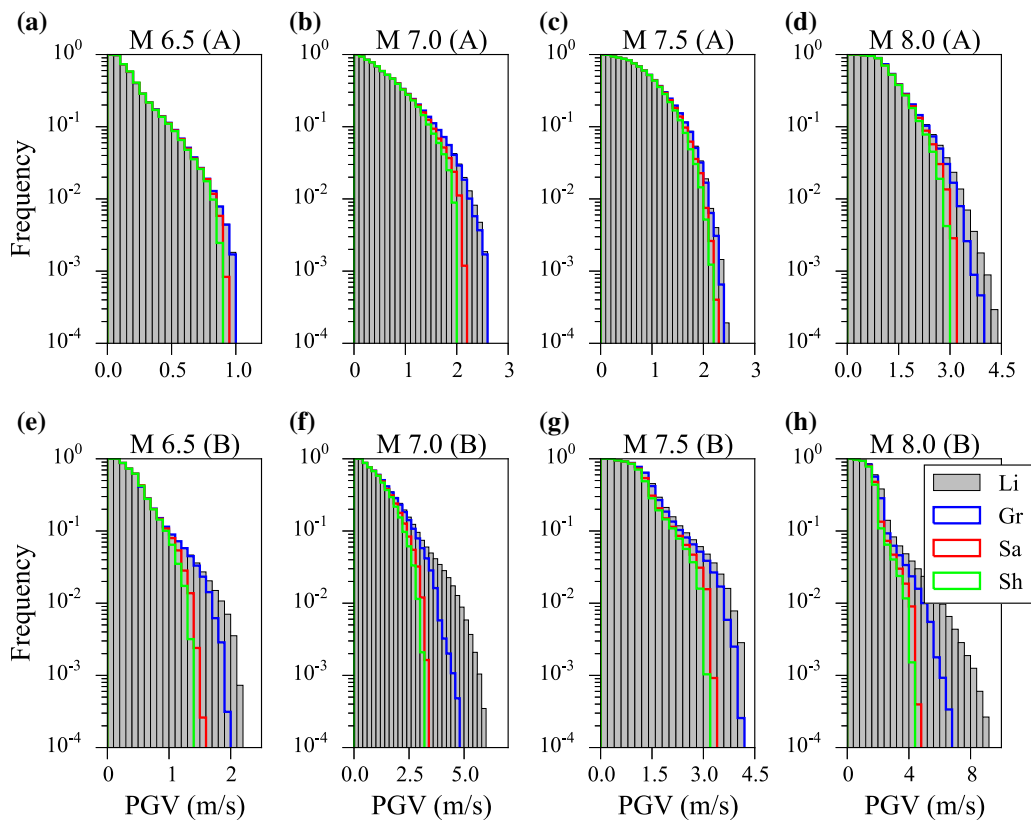


Figure 6

Cumulative frequency distribution of horizontal PGVs within 5 km of the fault for the four different scenario magnitudes and two different rupture models. *Gray filled bars* show linear results; while *colored lines* show non-linear results for the three rock strength models. *Li* linear, *Gr* granite, *Sa* sandstone, and *Sh* shale

plasticity occurs down to 4 and 5 km depth for the shale and sandstone models, respectively (Fig. 9e, f). Plasticity also breaks the symmetry across the fault (e.g., Andrews 2005), because the extensional side yields earlier than the compressive side.

4.2. Reduction of Near-Fault Ground Motions

The high near-surface PSRs caused by the LVZ translate into elevated mean PGVs in the vicinity of the fault in the linear case and for the granite

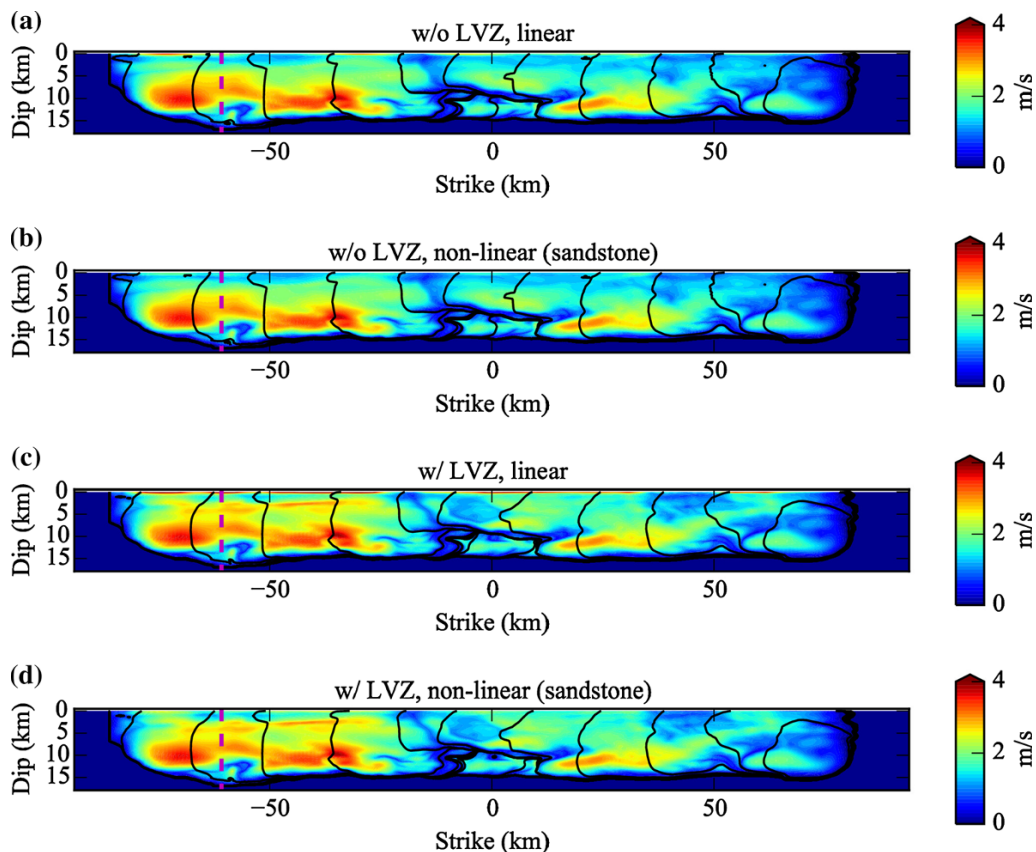


Figure 7

Peak slip rates obtained for the M 7.5 (rupture model A) scenario without LVZ in the **a** linear and **b** non-linear cases for the sandstone model, and with LVZ in the **c** linear and **d** non-linear cases for the sandstone model. *Solid black lines* show rupture times in 5 s intervals. The *dashed line* shows the location of the cross sections shown in Fig. 9

model (Fig. 10). Plasticity reduces near-fault PGVs as well as PSRs in the shale and sandstone model. As a result, near-fault ground motions are a lot more sensitive to the choice of rock strength in the scenarios which include an LVZ. At larger fault distances ($R_x > 2$ km), outside of the LVZ, mean PGVs are slightly lower in the simulations with an LVZ than in the simulations without it, even in the linear case. For example, mean PGVs at $R_x = 4$ km are ~ 0.5 m/s in the M 7 scenario without LVZ (Fig. 5b), but only 0.4 m/s in the scenario with LVZ (Fig. 10b), independent of rock strength. This reduction could be explained by trapping of waves inside the LVZ, which would reduce the amplitude of phases reaching regions outside the fault zone.

4.3. Effect of Non-linearity and LVZ On Fault-Zone Width

The deficit in coseismic near-surface slip, imposed by on-fault plasticity, is also clearly visible in the pattern of surface deformation across the fault (Fig. 11). The width of the fault zone, which is defined as the fault-perpendicular extent of observable surface shear on either side of the fault trace (e.g., Milliner et al. 2015), is sensitive to the choice of rock strength. In the linear case, and in the non-linear case for the granite model, the sign change in the fault-parallel displacement occurs abruptly, from about 1.4 m half a gridpoint south of the fault to -1.4 m half a grid point north of the fault (Fig. 11a). In contrast, in the non-linear

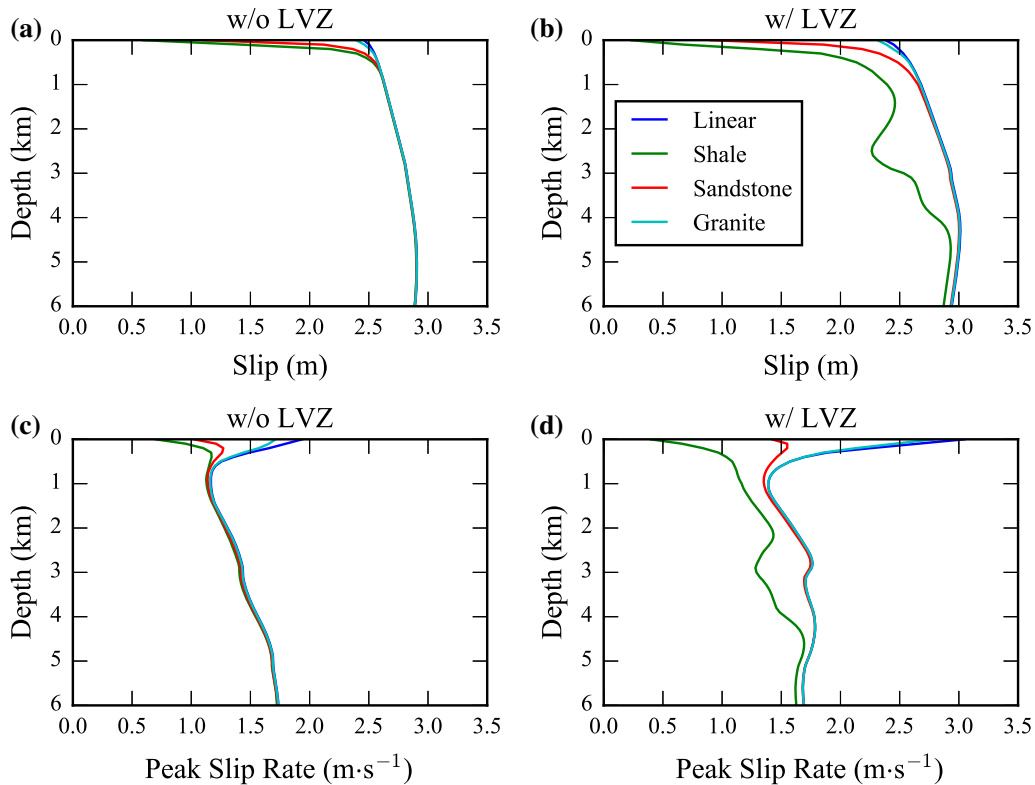


Figure 8

Average fault displacement obtained in M 7.5 (rupture model A) earthquake scenario **a** without and **b** with LVZ, and average peak slip rate **c** without and **d** with LVZ

case for the sandstone and shale models, the change occurs gradually over several grid points, resulting in a fault zone of finite width. The width of the fault zone is further increased if an LVZ is present (Fig. 11b). A fault zone of finite width is consistent with the deformation pattern derived from geodetic data, for example, for the 1992 M_w 7.3 Landers (Fig. 11c) earthquake (e.g., Fialko 2004; Milliner et al. 2015) or the 2003 M_w 6.5 Bam earthquake (e.g., Fialko et al. 2005).

The sensitivity of the fault-zone width to rock strength parameters may offer the prospect to constrain cohesions and friction angles in the fault damage zone by comparing the results of simulations against geodetic observations. Such comparisons will require detailed knowledge of the velocity structure in the damage zone, as well as simulations carried out with a smaller spatial discretization (25–50 m), to resolve the extent of the deformation zone.

5. Southern San Andreas Simulations

To assess the importance of plastic effects on ground motions during a realistic earthquake scenario, we performed dynamic simulations of an M 7.8 earthquake rupturing the southern San Andreas fault inside a 3-D heterogeneous velocity mesh (SCEC CVM 4, Magistrale et al. 2000). The scenario was first simulated w/o LVZ, then an LVZ was added to the CVM as described in Sect. 2.3. The computational domain was rotated clockwise by 27.5° to align the x-axis of the mesh with the San Andreas segment between Lake Hughes and the San Bernardino pass. We simulate a high stress drop event ($\overline{\Delta\tau} = 7.1$ MPa) rupturing the fault from SE to NW to mimic the M 7.8 ShakeOut scenario (Graves et al. 2008; Olsen et al. 2009). The total length of the rupture is 250 km, slightly shorter than the 300 km used for ShakeOut, with a magnitude of 7.74 and a maximum slip of 6 m. The initial stresses were computed in the same way as

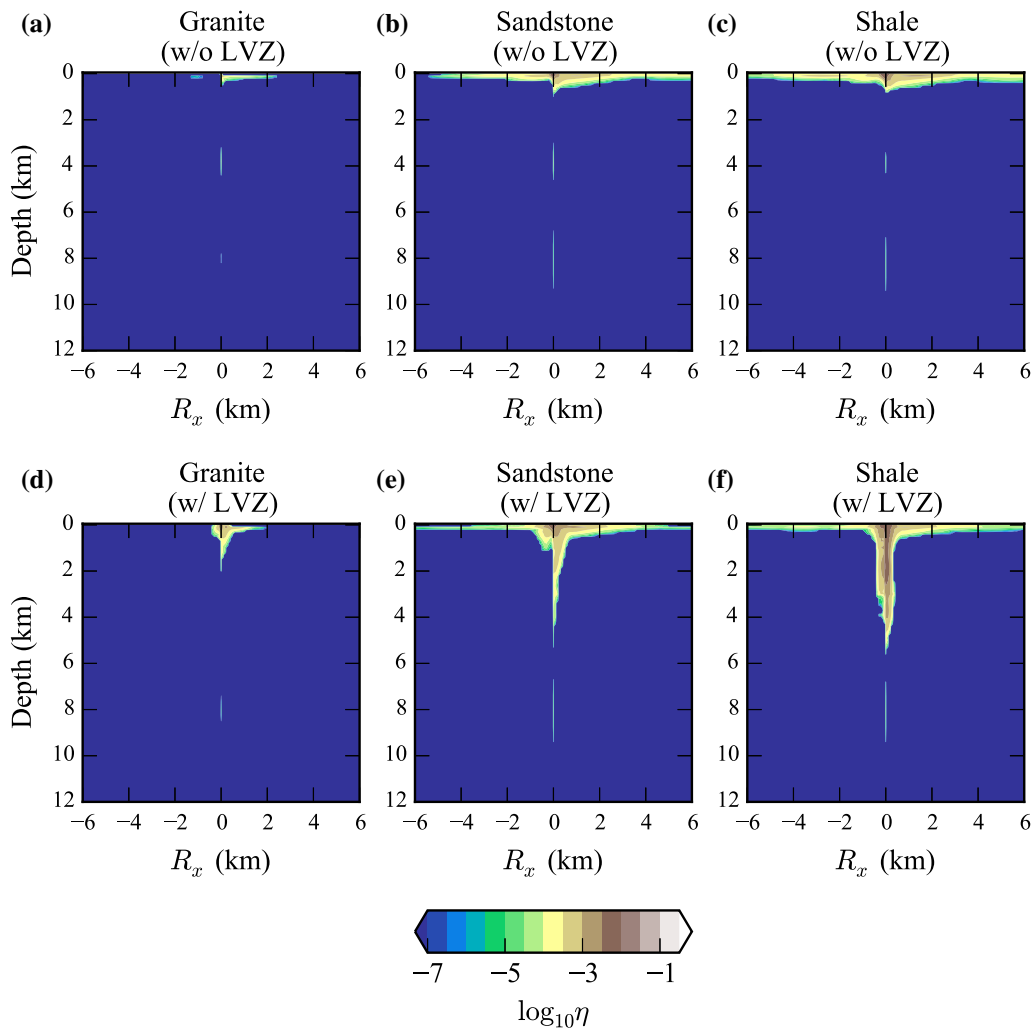


Figure 9

Accumulated plastic strain η on a cross section perpendicular to the fault at -60 km along strike (Fig. 7), obtained without LVZ for **a** granite, **b** sandstone, and **c** shale, and with LVZ for **d** granite, **e** sandstone, and **f** shale

in the previously described horizontally layered medium. We used $H = 0.50$ (Dalguer and Mai 2012; Baumann and Dalguer 2014), $\bar{\mu}_d = 0.30$, but increased $\bar{\mu}_s$ to 0.65 to prevent the occurrence of super-shear rupture (Andrews 1976). We used the same three rock strength models as in the simulations for the horizontally layered medium (Sect. 2.2), and plasticity was modeled using the granite, sandstone, and shale model throughout the computational domain. Although this is not a realistic assumption, the scope of these simulations was simply to analyze the sensitivity of ground motions to rock strength parameters. More accurate ground motion predictions

should assign Hoek–Brown parameters based on the the local geology, possibly in the framework of more detailed community structure models.

5.1. Results w/o LVZ

Figure 12a shows ground motions obtained without LVZ for a linear medium. Strong shaking ($\text{PGV} > 3$ m/s) occurs close to the fault, especially where the fault intersects the deep San Bernardino Basin. Pockets of strong shaking ($\text{PGV} > 1.5$ m/s) and long duration appear also in the San Gabriel valley and the

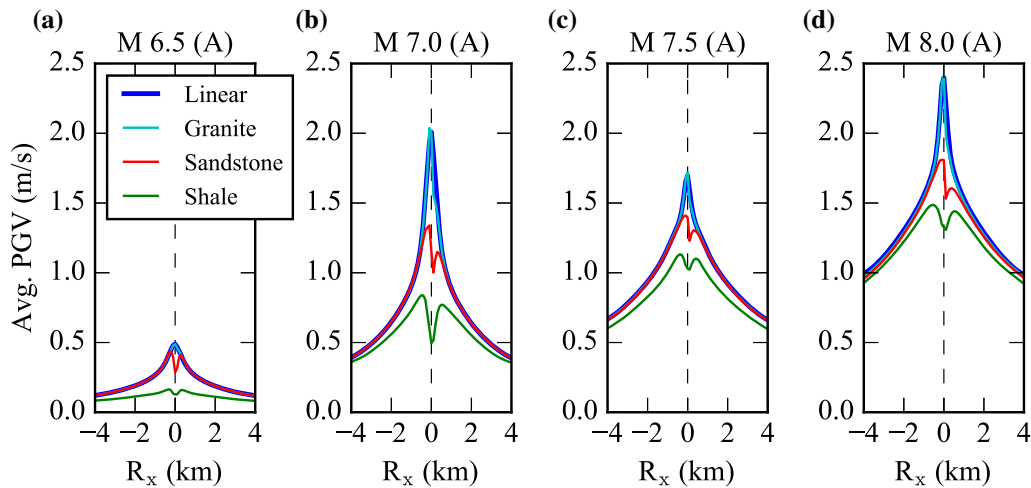


Figure 10

Same as Fig. 5, but showing results obtained with LVZ (rupture model A)

Los Angeles basin. These features were also observed in the ShakeOut simulations, and attributed to channeling of seismic waves along a string of sedimentary basins (Olsen et al. 2009). The presence of this waveguide amplification effect has also been confirmed from measurement of the ambient seismic noise (Denolle et al. 2013).

Non-linear simulations yield significantly lower shaking levels in the Whittier Narrows corridor (at station ‘rus’ in Fig. 12), where PGVs are reduced from more than 2 m/s to less than 1.75 m/s for the granite model (Fig. 12b) and to less than 1.25 m/s for the shale model (Fig. 12c). Plastic effects are also pronounced in the San Gabriel valley (NE of site ‘lab’) where PGVs are reduced from ~ 1.75 m/s in the linear prediction to less than 1.0 m/s for the shale model. These reductions are comparable to those reported for kinematic ShakeOut simulations with plasticity (Roten et al. 2014).

Figure 13a shows the distribution of PGVs inside a rectangular area, including the San Gabriel and Los Angeles basins (dashed area in Fig. 12). In addition to reducing the occurrence of PGVs above 1.0 m/s, non-linearity results in a shift of the entire distribution towards lower values: Average PGVs inside the selected area are reduced from 0.56 m/s for the visco-elastic case to 0.48, 0.40, and 0.37 m/s in the visco-plastic case using the granite, sandstone, and shale models, respectively.

Inside the San Bernardino basin, within 20 km of the fault (Fig. 13b), PGVs are also asymmetrically

distributed around the average values (1.55 m/s in the linear case, 1.38 m/s in granite, 1.28 m/s in sandstone, and 1.24 m/s in shale). The probability densities exhibit a long tail, with PGVs exceeding 6 m/s in the linear case. Here, plasticity acts mostly by truncating the tail of the frequency distribution, with the truncation level depending on the choice of rock strength: extreme PGVs are reduced to less than 5 m/s for the granite and less than 4 m/s for the sandstone and shale models.

5.2. Results w/ LVZ

The San Andreas simulations were repeated for a mesh including an LVZ for the linear case and the non-linear cases with all three rock strength models. Figure 14a shows the change in PGVs resulting from including the LVZ in the linear case. Because the LVZ affects the dynamics of the rupture, the pattern is heterogeneous, with the LVZ reducing PGVs in some regions and increasing them in others. Fault-zone trapped waves may lead to further increased ground motions in the vicinity of the fault. On soft basins characterized by trapping effects, especially along the waveguide connecting the San Andreas fault with the Los Angeles basin, reductions tend to dominate. Compared to the linear simulations w/o LVZ (Fig. 13a, b), the distribution of linear PGVs in the Los Angeles and San Bernardino basins is more compact if the LVZ is included (Fig. 13c, d).

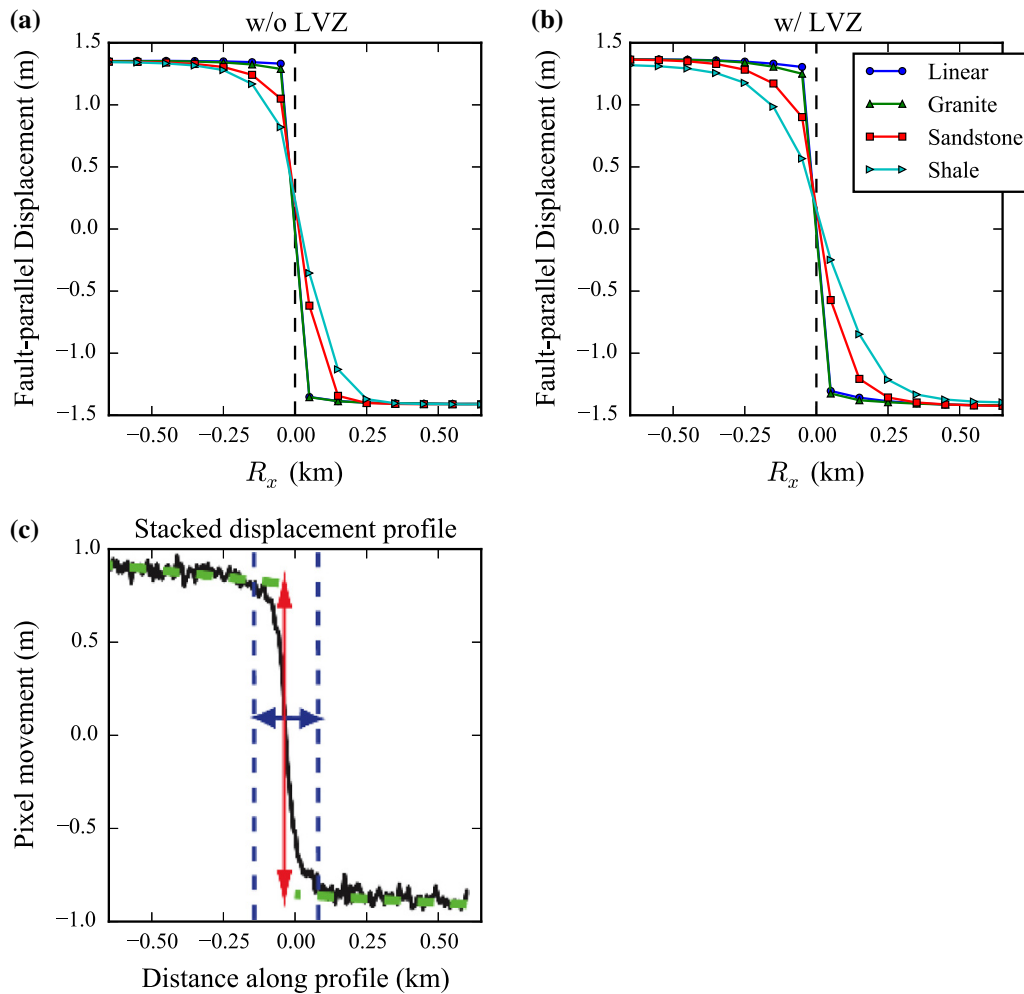


Figure 11

Mean fault-parallel displacement obtained from dynamic simulations of M_w 7.5 earthquake using different rock strength models **a** without and **b** with an LVZ. **c** Fault-parallel displacement derived for the 1992 M_w 7.3 Landers earthquake from stacked aerial images by Milliner et al. (2015). Dashed blue lines outline the width of the fault zone. (Modified from Milliner et al. 2015)

If plastic yielding is considered, the amount of these reductions is further increased, especially in the sandstone and shale model (14b). PGV distributions resulting from the shale model are clearly more consolidated than those obtained with the sandstone model (Fig. 13c, d), while these two models yield quite similar results w/o the LVZ (Fig. 13a, b). This pattern reflects the distribution of yield strength with depth obtained with and without the LVZ in the sandstone and shale models (Fig. 2).

For the granite model, amplifications caused by fault-zone trapped waves take precedence over non-linear attenuation in the fault damage zone, and PGVs

above 5 m/s are more frequent with the LVZ than without near the fault in the San Bernardino basin (Fig. 13d). However, as noted earlier, the combination of low shear-wave velocity and high rock strength in the fault damage zone is likely not realistic, and neither is the assumption of linear behavior.

5.3. Comparison of Spectral Accelerations Against Ground Motion Prediction Equations

In the preceding analysis, we have only analyzed the effects of plasticity on peak ground velocities.

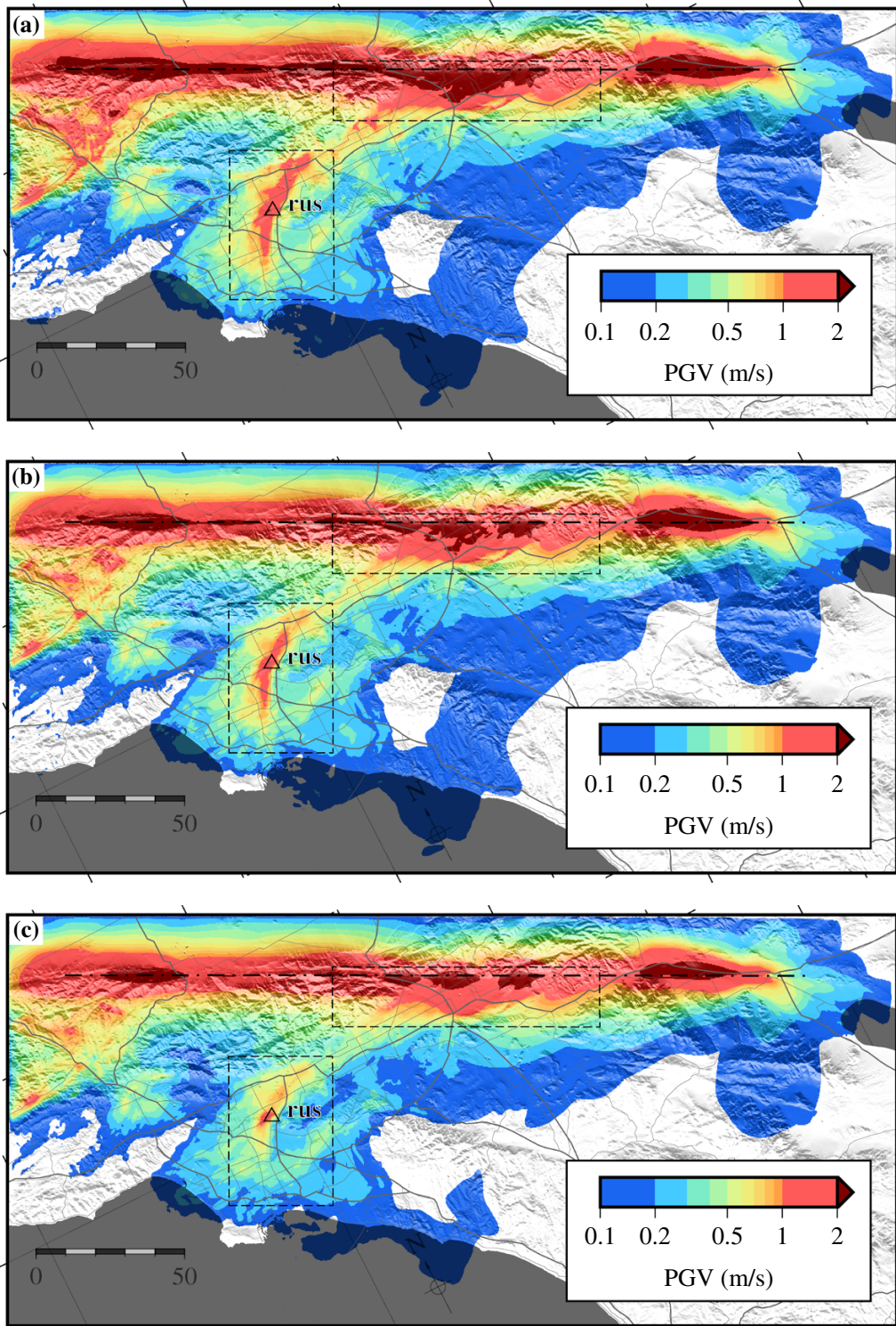


Figure 12

PGVs for southern San Andreas $M 7.8$ scenario obtained in **a** linear media, **b** granite, and **c** shale. The dash-dotted line shows the fault; dashed rectangles show regions used for Fig. 13

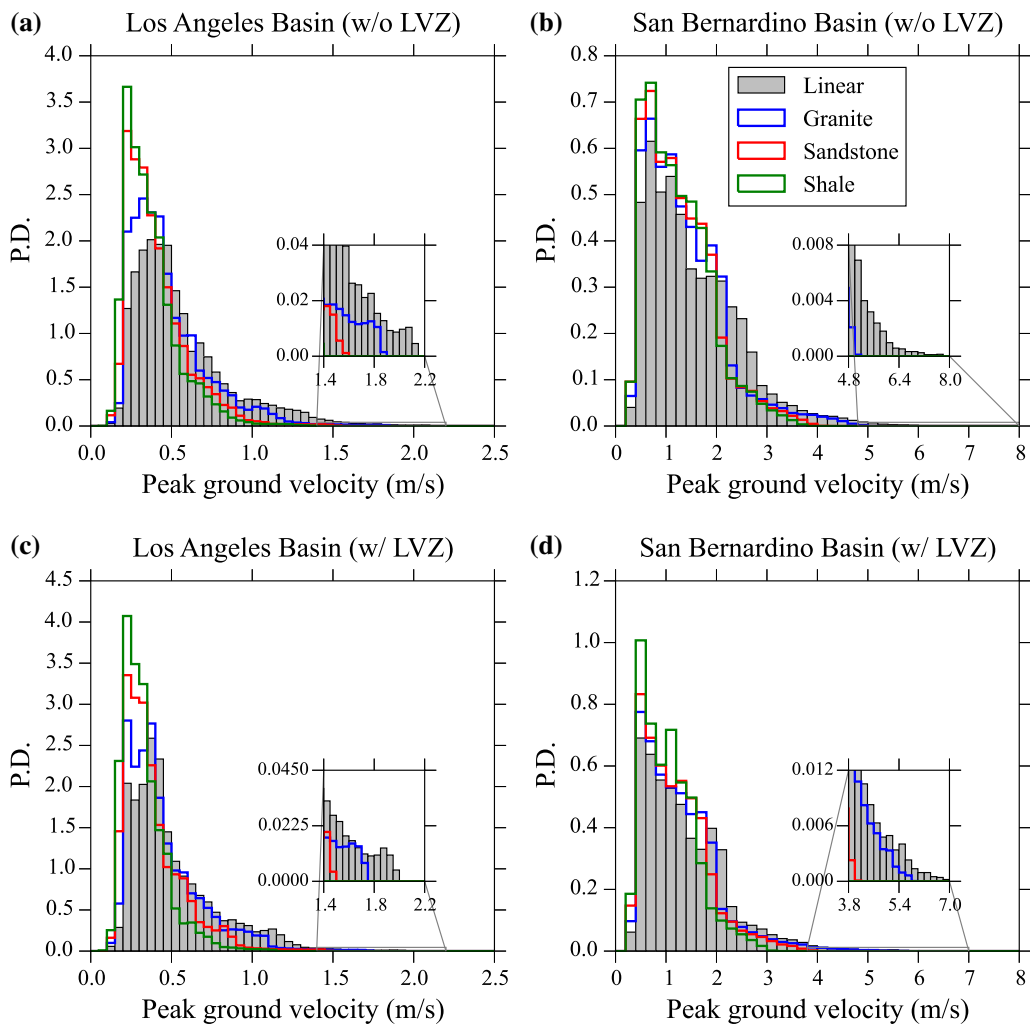


Figure 13

Histograms with PGVs resulting from an M 7.8 event on southern San Andreas fault in a linear (visco-elastic) medium and in non-linear media using different rock strength models. **a** Area around Los Angeles basin, w/o LVZ. **b** Near-fault area, including Bernardino basin, w/o LVZ. **c** Same as **a**, w/ LVZ. **d** Same as **b**, w/ LVZ (see Fig. 12 for selected areas). *P.D.* probability density

Although PGVs are typically reflecting the intermediate frequency content of the signal, they can also be controlled by high-frequency phases. To analyze the effects of plasticity at different frequencies, we computed spectral accelerations from synthetics for the San Andreas scenario including the LVZ. Figure 15 compares maps with spectral accelerations at a period of 3 s (3s-SAs) obtained from the linear simulation and the non-linear simulation using the sandstone model.

The distribution of 3s-SAs follows a similar pattern as PGVs. In the linear case, 3s-SAs exceed 1 g on the

soft sediments of the San Bernardino basins and Imperial valley in the vicinity of the fault (Fig. 15a). We also record values in excess of 0.5 g along the San Bernardino–Los Angeles basin waveguide, and even 0.8 g at Whittier narrows. In the non-linear case for the sandstone model (Fig. 15b), near-fault 3s-SAs remain below 1 g, and 0.5 g are exceeded within a much smaller area inside the waveguide.

We compare SAs obtained from these dynamic simulations against two recent ground motion prediction equations (GMPEs) along two profiles, with one profile representing rock sites and one profile

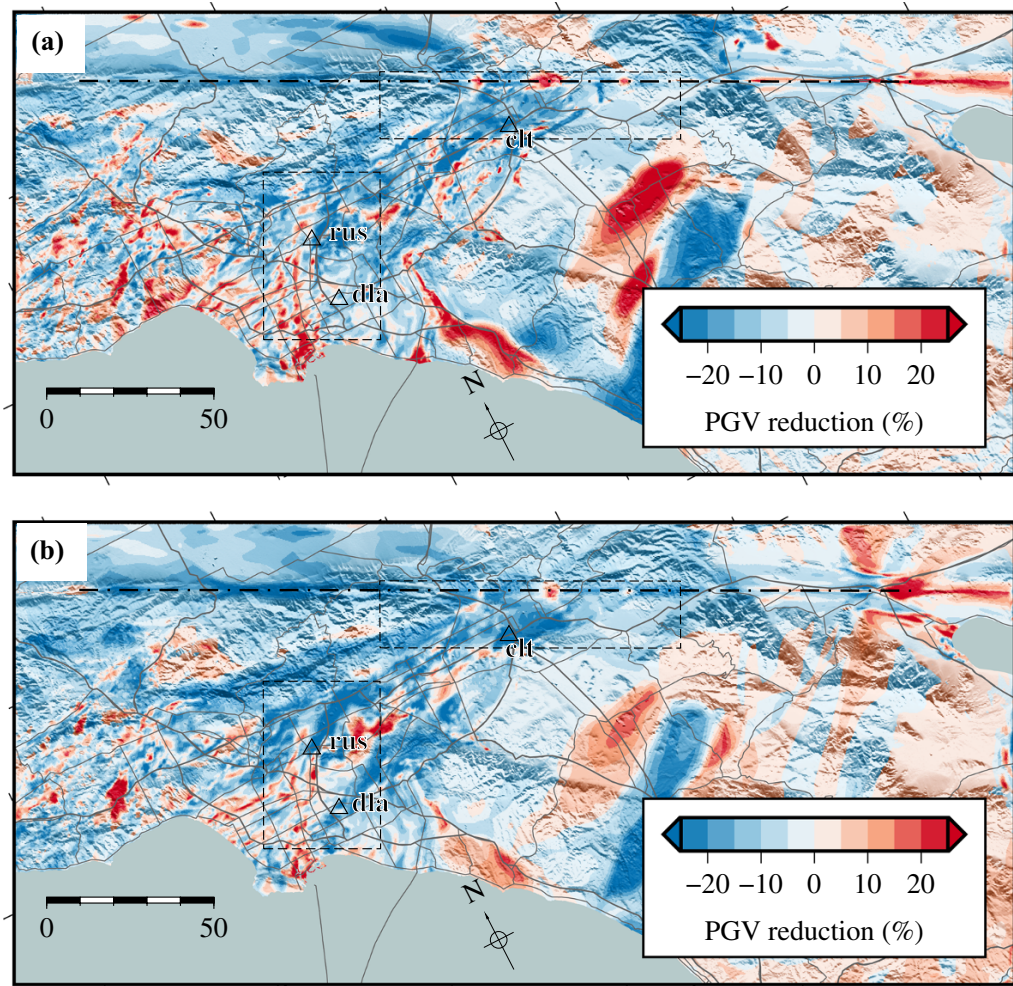


Figure 14

Change in PGV obtained from San Andreas simulation, including a LVZ, with respect to scenario without LVZ, in **a** linear case and **b** non-linear case for shale model. (Blue areas indicate that an LVZ results in lower PGVs)

representing soft soil sites (see Fig. 15 for site locations). We used the GMPEs of Boore et al. (2014) and Campbell and Bozorgnia (2014), which will be referred to as BSSA14 and CB14, respectively, through the remainder of the text. Both equations require the basin depth z_1 , which is the isosurface where the shear-wave velocity v_s reaches 1000 m/s; in addition, CB14 requires the depth to the $v_s = 2500$ m/s isosurface, $z_{2.5}$. We extracted the depth of these surfaces from the CVM for each site along the two cross sections. For the rock sites, we used a $v_{s,30}$ (average shear-wave velocity in the top 30 m) of 760 m/s (a value commonly used for rock sites, e.g., Olsen et al. 2008), while a $v_{s,30}$ of 250 m/s was used

for the soil sites. (These values are lower than the near-surface v_s used in the simulations, which used a minimum shear-wave velocity of 500 m/s and rock velocities above 1500 m/s. The logic behind these $v_{s,30}$ choices is that realistic rock sites include a low-velocity weathered layer, which was not included in our simulations, as it would be too shallow to influence long-period spectral accelerations. Likewise, typical soil sites are characterized by very low shear-wave velocities in top few meters, which result in lower $v_{s,30}$ than the 500 m/s used in our simulations. However, these shallow low-velocity layers would not be resolvable using the 100 m-grid spacing in our simulations. The same reasoning has been used

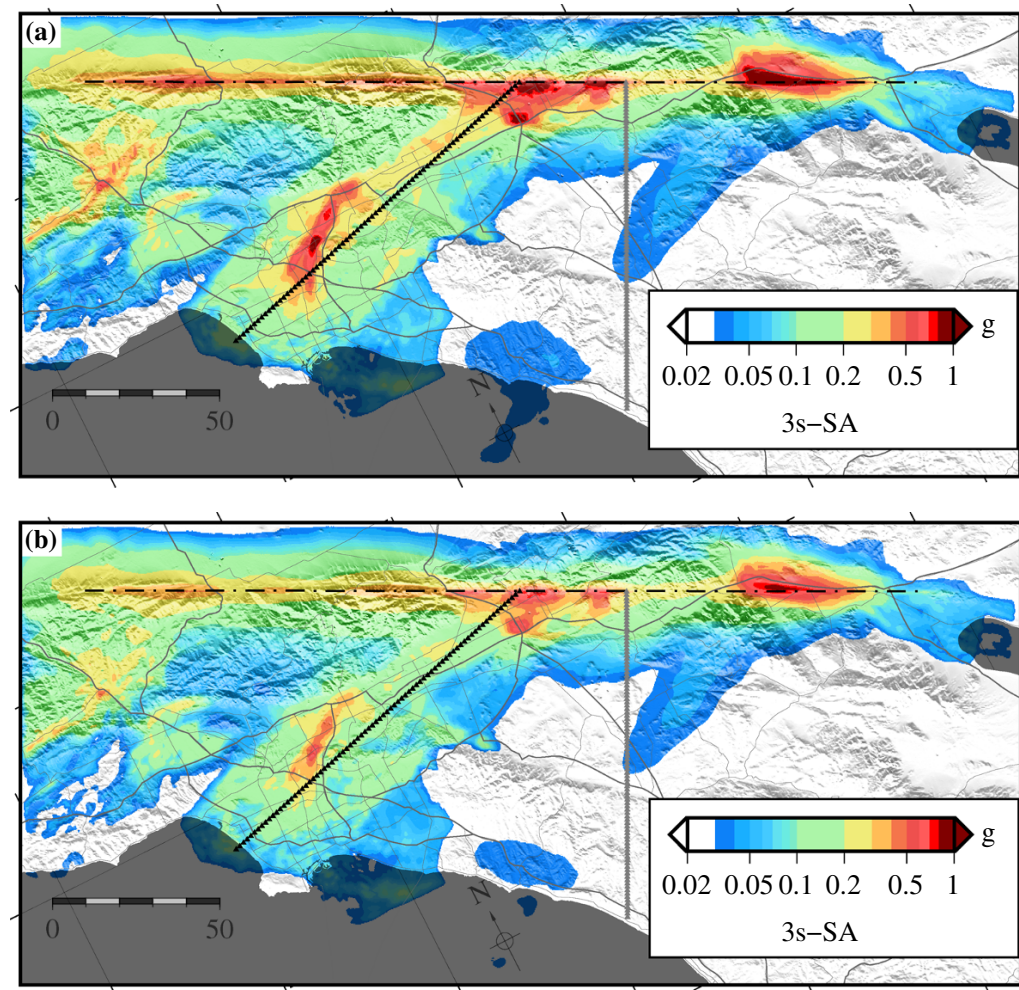


Figure 15

Spectral accelerations at 3 s obtained for **a** linear simulation and **b** non-linear simulation using the sandstone model in the M 7.8 southern San Andreas scenario, including an LVZ. Gray triangles show rock sites and black triangles soil sites used in the comparison against GMPEs (Figs. 16, and 17, respectively)

in the previous comparisons of simulations against GMPEs, e.g., Olsen et al. 2008).

Along the cross section for the rock sites (Fig. 16), effects of plasticity are more pronounced at 2s-SAs than at 3s-SAs; reductions are significant for the shale model at 3s, while both the sandstone and shale model show pronounced plastic effects at 2s. At distances above ~ 10 km, both linear and non-linear models are generally within one standard deviation of the values predicted by the two GMPEs. Close to the fault ($R_x < 10$ km), the GMPEs are exceeded by more than one standard deviation except in the non-linear case for the shale model.

Along the cross section on the soft fill of the San Bernardino, San Gabriel, and Los Angeles basins, both simulated and GMPE-derived SAs show more variability with distance, reflecting changes in local basin depth (Fig. 17). Linear 3s-SAs exceed both BSSA14 and CB14 at fault distances between ~ 40 and ~ 70 km. Accounting for non-linearity brings the 3s-SAs closer to the GMPE values; however, both BSSA14 and CB14 are still exceeded by more than one standard deviation where the cross section traverses the waveguide, approximately 55 km from the fault (Fig. 17a, b). This waveguide amplification, which has a dominant period near 4.5 s (Olsen et al. 2006),

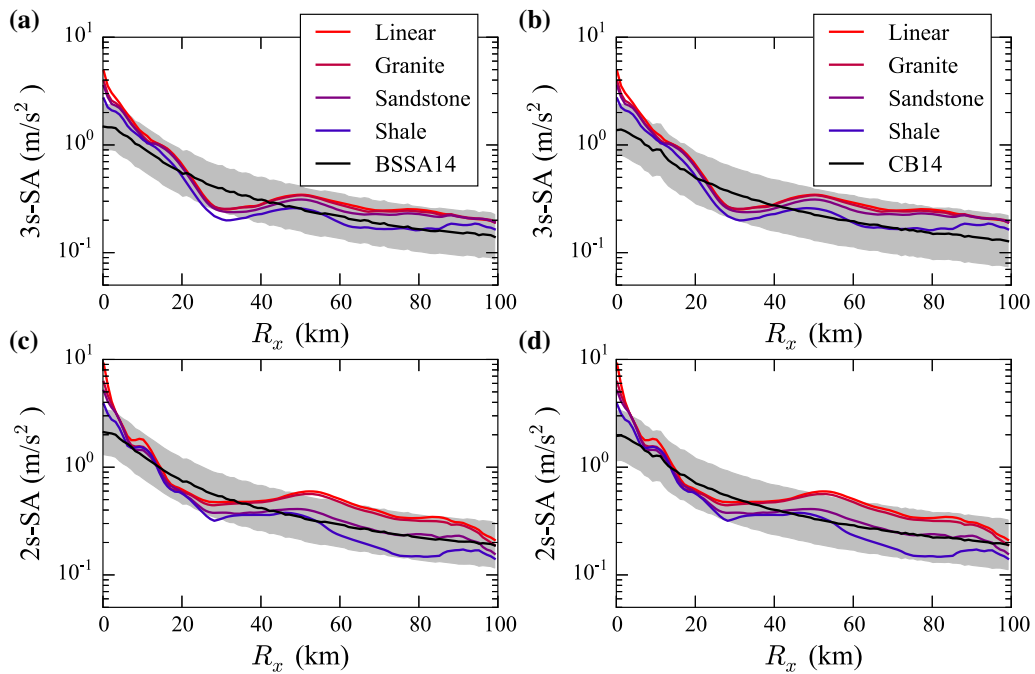


Figure 16

Spectral accelerations as a function of distance for rock sites (Fig. 15) compared against two GMPEs, including the interval within 84–16% exceedance probability (gray shaded areas). **a** Simulated 3s-SAs vs. BSSA14, **b** 3s-SAs vs. CB14, **c** 2s-SAs vs. BSSA14, and **d** 2s-SAs vs. CB14

is less visible on 2s-SAs (Fig. 17c, b). Synthetic ground motions obtained with the sandstone and shale model are mostly within the 84% confidence interval of the CB14 predictions (Fig. 17d).

6. Conclusions

Our simulations suggest that non-linear effects may be relevant at frequencies below 1 Hz, and at magnitudes as low as 6.5. In terms of average PGVs directly above the fault (Table 3), the reduction (with respect to a linear simulation) is not very sensitive to the scenario magnitude, but more sensitive to the amount of stress drop. For moderate stress drop earthquakes ($\Delta\tau \approx 3$ MPa), effects of plasticity on mean peak ground velocities are not significant at distances of a few kilometers from the fault, unless a damage zone filled with poor quality (strongly pre-fractured) rock is present. However, plasticity reduces the intra-event variability of ground motions by limiting the occurrence of extreme shaking. With respect to truncation of

frequency-distribution curves (Fig. 6), the dependence on scenario magnitude is more pronounced than for average ground motions. However, more simulations will have to be carried out, with different realizations of the initial stress on the fault, to assess the magnitude dependence of plastic effects. Effects of plasticity are exacerbated if a damage zone, characterized by reduced shear-wave velocities and reduced rock strength, has evolved around the fault.

Simulations of a high stress drop M 7.8 scenario earthquake on the southern San Andreas fault for a realistic earth structure, including an LVZ demonstrate that plastic effects can be relevant at periods of 2 and 3 s, especially on soft soils. Spectral accelerations at 2 and 3 s obtained in our non-linear models are consistent with two recent GMPEs for both rock and soil sites; indeed, long-period ground motions in the Los Angeles basin agree better with GMPEs if plasticity is considered.

Plastic effects are especially important close to the surface (e.g., Roten et al. 2014), and the reduction of peak slip rates is most pronounced in the shallow part of the fault (Fig. 4f). Velocity-strengthening fault

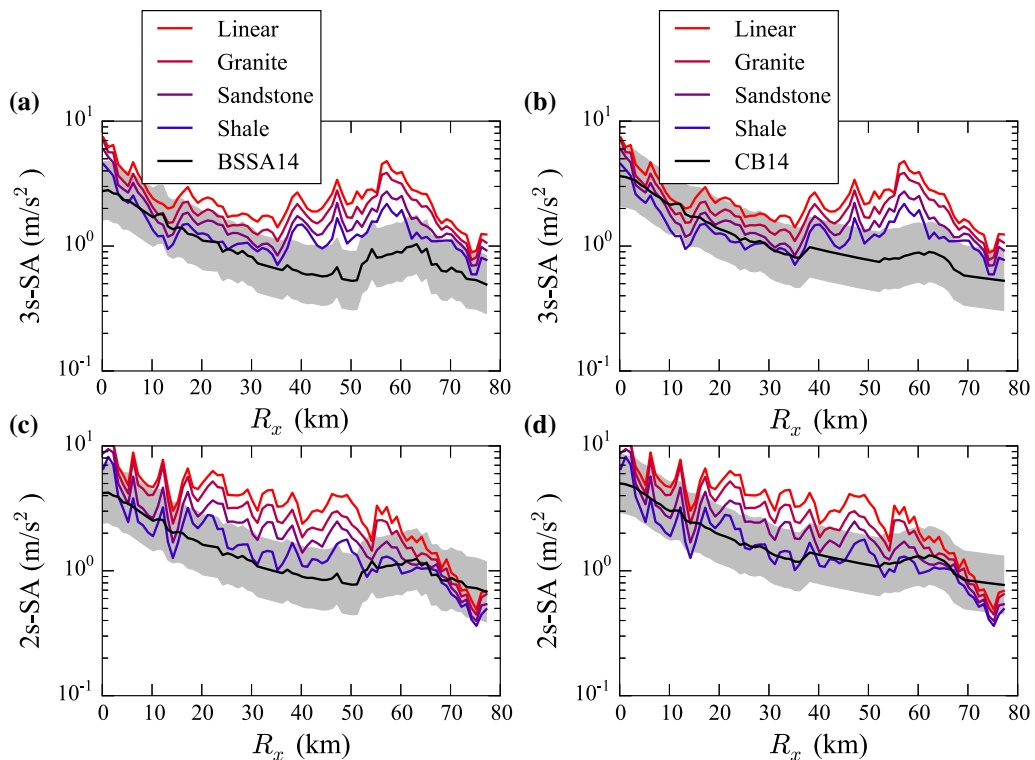


Figure 17

Same as Fig. 17, but showing comparison along profile for soil sites (Fig. 15)

friction in the uppermost brittle crust may reduce the final slip and peak slip rates in a similar way. Although rate strengthening is not yet implemented in AWP-ODC, its effects have been emulated in the previous studies (e.g., Dalguer and Mai 2012; Roten et al. 2011; Baumann and Dalguer 2014) by increasing the critical slip distance or by tapering off the shear stress near the surface. In this work, we did deliberately not emulate velocity strengthening in our rupture models to avoid masking effects of plasticity. However, effects of near-surface non-linearity may, at least in part, be emulated by adding velocity strengthening, or more generally by imposing a limit on slip velocity near the surface (Andrews 2005). For moderate stress drop earthquakes, physically meaningful mean PGVs can be predicted using linear simulations at distances beyond ~ 1 km from the fault. However, care should be taken to control peak slip rates near the surface, for example by increasing the value of the critical slip distance at shallow depth (e.g., Olsen et al. 2008). This is particularly important if a low-velocity damage zone filled with pre-fractured rock is present.

Ongoing research is directed at developing criteria for emulating plasticity by modifying source time functions in linear rupture models. Future simulations should also include non-surface-rupturing scenarios to investigate the sensitivity of plastic effects on rupture depth (Dalguer et al. 2008b).

Simulations presented in this work were performed for three rock strength models representing good, average, and poor quality rocks. The sensitivity of ground motions to the presence of a fault damage zone, characterized by laterally varying degrees of fracturing, demonstrates the importance of developing more sophisticated, heterogeneous representations that define the strength of crustal and sedimentary rocks inside community velocity models. In particular, such models should distinguish between rock and unconsolidated sediments, because the Hoek–Brown criterion was not developed to describe the strength of soil. The cohesions of unconsolidated sediments in the San Bernardino and Los Angeles basins might be even lower than described in our shale model, which would further reduce long-period ground motions in these areas.

Acknowledgements

Computations were performed on Blue Waters at NCSA, using resources provided through the PRAC (Petascale Computing Resource Allocation) program, and on Titan, which is part of the Oak Ridge Leadership Facility at the Oak Ridge National Laboratory supported by DOE Contract No. DE-AC05-00OR22725. This research was supported by SCEC through by NSF Cooperative Agreement EAR-0529922 and USGS Cooperative Agreement 07HQAG0008, by USGS award G15AP00077, and by NSF awards EAR-1226343, OCI-114849, OCI-1450451, and EAR-1135455. We used the PyNGA package for Python by Feng Wang to compute spectral accelerations predicted by the two GMPEs. The authors thank two anonymous reviewers and the guest editor for valuable suggestions that helped to improve the manuscript.

REFERENCES

- Andrews, D. (1976). Rupture velocity of plane strain shear cracks. *Journal Geophysical Research*, 81(32), 5679–5687.
- Andrews, D. (2005). Rupture dynamics with energy loss outside the slip zone. *Journal of Geophysical Research*, 110(B1), 307.
- Andrews, D., Hanks, T., & Whitney, J. (2007). Physical limits on ground motion at Yucca Mountain. *Journal Geophysical Research*, 97(6), 1771–1792.
- Barall, M. (2010). *Tpv26 and tpv27 vertical fault with viscoplasticity benchmarks*. Report: Invisible Software Inc.
- Baumann, C., & Dalguer, L. (2014). Evaluating the compatibility of dynamic rupture-based synthetic ground motion with empirical ground-motion prediction equation. *Bulletin of the Seismological Society of America*, 104(2),
- Bizzarri, A. (2010). How to promote earthquake ruptures: Different nucleation strategies in a dynamic model with slip-weakening friction. *Journal Geophysical Research*, 100(3), 923–940.
- Bommer, J., & Abrahamson, N. (2006). Why do modern probabilistic seismic-hazard analyses often lead to increased hazard estimates? *Journal Geophysical Research*, 96(6), 1967–1977.
- Bommer, J., Abrahamson, N., Strasser, F., Pecker, A., Bard, P.-Y., Bungum, H., et al. (2004). The challenge of defining upper bounds on earthquake ground motions. *Journal Geophysical Research*, 75(1), 82–95.
- Boore, D. M., Stewart, J. P., Seyhan, E., & Atkinson, G. M. (2014). NGA-West2 equations for predicting PGA, PGV, and 5% damped PSA for shallow crustal earthquakes. *Journal Geophysical Research*, 30(3), 1057–1085.
- Campbell, K. W., & Bozorgnia, Y. (2014). NGA-West2 ground motion model for the average horizontal components of PGA, PGV, and 5% damped linear acceleration response spectra. *Journal Geophysical Research*, 30(3), 1087–1115.
- Chang, C., Zoback, M. D., & Khaksar, A. (2006). Empirical relations between rock strength and physical properties in sedimentary rocks. *Journal Geophysical Research*, 51(3), 223–237.
- Cochran, E. S., Li, Y.-G., Shearer, P. M., Barbot, S., Fialko, Y., & Vidale, J. E. (2009). Seismic and geodetic evidence for extensive, long-lived fault damage zones. *Geology*, 37(4), 315–318.
- Cui, Y., Olsen, K., Lee, K., Zhou, J., Small, P., Roten, D., Ely, G., Panda, D., Chourasia, A., Levesque, J., Day, S., & Maechling, P. (2010). Scalable earthquake simulation on petascale supercomputers. In *Proceedings of SC10*. New Orleans, LA.
- Dalguer, L., & Day, S. (2007). Staggered-grid split-node method for spontaneous rupture simulation. *Journal of Geophysical Research*, 112(B02), 302.
- Dalguer, L., & Mai, P. (2012). Prediction of near-source ground motion exceeding 1g at low frequencies (< 2 Hz) from $M_w \sim 6.5$ deterministic and numerical simulations physics-based dynamic rupture simulations. In *Proceedings of 15th World Conference on Earthquake Engineering*. Lisbon: Int. Assoc. for Earthquake Eng.
- Dalguer, L., Day, S., Olsen, K., & Cruz-Atienza, V. (2008a). Rupture models and ground motion for Shakeout and other southern San Andreas fault scenarios. In *Proceedings of 14th World Conference on Earthquake Engineering*. Beijing: Int. Assoc. for Earthquake Eng.
- Dalguer, L. A., & M. Mai. (2008). Implications of Style-of-Faulting and Loading Characteristics on the Dynamic Rupture Process. In *AGU Fall Meeting Abstracts* (pp. D1798).
- Dalguer, L. A., Miyake, H., Day, S. M., & Irikura, K. (2008b). Surface rupturing and buried dynamic-rupture models calibrated with statistical observations of past earthquakes. *Geology*, 98(3), 1147–1161.
- Day, S., & Bradley, C. (2001). Memory-efficient simulation of anelastic wave propagation. *Geology*, 91(3), 520.
- Denolle, M., Dunham, E., Prieto, G., & Beroza, G. (2013). Strong Ground Motion Prediction using Virtual Earthquakes. *Science*, 343, 2013.
- Duan, B., & Day, S. (2010). Sensitivity study of physical limits on ground motion at Yucca Mountain. *Science*, 100(6), 2996–3019.
- Dunham, E. M., Belanger, D., Cong, L., & Kozdon, J. E. (2011a). Earthquake ruptures with strongly rate-weakening friction and off-fault plasticity, Part 1: planar faults. *Science*, 101(5), 2296–2307.
- Dunham, E. M., Belanger, D., Cong, L., & Kozdon, J. E. (2011b). Earthquake ruptures with strongly rate-weakening friction and off-fault plasticity, Part 2: Nonplanar faults. *Science*, 101(5), 2308–2322.
- Fialko, Y. (2004). Probing the mechanical properties of seismically active crust with space geodesy: Study of the coseismic deformation due to the 1992 M_w 7.3 Landers (southern California) earthquake. *Journal of Geophysical Research: Solid Earth*, 109(B3),
- Fialko, Y., Sandwell, D., Simons, M., & Rosen, P. (2005). Three-dimensional deformation caused by the Bam. *Science*, 435(7040), 295–299.
- Field, E., Kramer, S., Elgamal, A.-W., Bray, J., Matasovic, N., Johnson, P., et al. (1998). Nonlinear site response: Where we're at (a report from a SCEC/PEER seminar and workshop). *Science*, 69(3), 230–234.
- Gabriel, A.-A., Ampuero, J.-P., Dalguer, L. A., & Mai, P. M. (2013). Source properties of dynamic rupture pulses with off-

- fault plasticity. *Journal Geophysical Research*, 118(8), 4117–4126. doi:10.1002/jgrb.50213.
- Graves, R., & R. Pitarka. (2016). Kinematic ground motion simulations on rough faults including effects of 3D stochastic velocity perturbations. *Bulletin of the Seismological Society of America* (submitted to).
- Graves, R. W., Aagaard, B. T., Hudnut, K. W., Star, L. M., Stewart, J. P., & Jordan, T. H. (2008). Broadband simulations for Mw 7.8 southern San Andreas earthquakes: Ground motion sensitivity to rupture speed. *Geophysical Research Letters*, 35(22), 302.
- Hanks, T., Abrahamson, N., Board, M., Boore, D., Brune, J., & Cornell, C. (2005). Observed ground motions, extreme ground motions, and physical limits to ground motions. In *Directions in Strong Motion Instrumentation* (pp. 55–59).
- Harris, R., Barall, M., Archuleta, R., Dunham, E., Aagaard, B., Ampuero, J., et al. (2009). The SCEC/USGS dynamic earthquake rupture code verification exercise. *Journal Geophysical Research*, 80(1), 119–126.
- Harris, R. A., & Day, S. M. (1997). Effects of a low-velocity zone on a dynamic rupture. *Journal Geophysical Research*, 87(5), 1267–1280.
- Harris, R. A., Barall, M., Andrews, D., Duan, B., Ma, S., Dunham, E., et al. (2011). Verifying a computational method for predicting extreme ground motion. *Journal Geophysical Research*, 82(5), 638–644.
- Hoek, E., Carranza-Torres, C., & Corkum, B. (2002). Hoek-Brown failure criterion - 2002 edition. *Journal Geophysical Research*, 1, 267–273.
- Horsrud, P. (2001). Estimating mechanical properties of shale from empirical correlations. *Journal Geophysical Research*, 16(2), 68–73.
- Huang, Y., Ampuero, J.-P., & Helmberger, D. V. (2014). Earthquake ruptures modulated by waves in damaged fault zones. *Journal Geophysical Research*, 119(4), 3133–3154.
- Leonard, M. (2010). Earthquake fault scaling: self-consistent relating of rupture length, width, average displacement, and moment release. *Journal Geophysical Research*, 100(5A), 1971–1988.
- Li, Y. G., Vidale, J. E., & Cochran, E. S. (2004). Low-velocity damaged structure of the San Andreas Fault at Parkfield from fault zone trapped waves. *Geophysical Research Letters*, 31(12), 1267–1270.
- Ma, S. (2008). A physical model for widespread near-surface and fault zone damage induced by earthquakes. *Geochemistry Geophysics Geosystems*, 9(11), 009.
- Ma, S., & Andrews, D. (2010). Inelastic off-fault response and three-dimensional dynamics of earthquake rupture on a strike-slip fault. *Journal of Geophysical Research: Solid Earth*, 115(B4), B04301.
- Magistrale, H., Day, S., Clayton, R., & Graves, R. (2000). The SCEC Southern California Reference Three-Dimensional Seismic Velocity Model Version 2. *Journal Geophysical Research*, 90(6B), S65–S76.
- Mai, P. M., & Beroza, G. C. (2002). A spatial random field model to characterize complexity in earthquake slip. *Journal of Geophysical Research (Solid Earth)*, 107, 2308.
- Marinos, V., Marinos, P., & Hoek, E. (2005). The geological strength index: applications and limitations. *Journal Geophysical Research*, 64(1), 55–65.
- Milliner, C., Dolan, J., Hollingsworth, J., Leprince, S., Ayoub, F., & Sammis, C. (2015). Quantifying near-field and off-fault deformation patterns of the 1992 Mw 7.3 Landers earthquake. *Geochemistry, Geophysics, Geosystems*, 16, 1577–1598.
- Olsen, K. B. (1994). Simulation of three-dimensional wave propagation in the Salt Lake basin, Ph.D. thesis, University of Utah, Salt Lake City, Utah.
- Olsen, K. B., Day, S. M., Minster, J. B., Cui, Y., Chourasia, A., Faerman, M., et al. (2006). TeraShake: Strong shaking in Los Angeles expected from southern San Andreas earthquake. *Journal Geophysical Research*, 77, 281–282.
- Olsen, K. B., Day, S. M., Minster, Y. A., Cui, Y., Chourasia, A. J., Okaya, D., & Maechling, P. (2008). Terashake2; spontaneous rupture simulations of Mw 7.7 earthquakes on the southern San Andreas Fault. *Bulletin of the Seismological Society of America*, 98(3), 1162–1185, 2008.
- Olsen, K. B., Day, S. M., Dalguer, L. A., Mayhew, J., Cui, Y., Zhu, J., et al. (2009). ShakeOut-D: Ground motion estimates using an ensemble of large earthquakes on the southern San Andreas fault with spontaneous rupture propagation. *Geophysical Research Letters*, 36(4), 303.
- Roten, D., Olsen, K. B., Pechmann, J., Cruz-Atienza, V., & Magistrale, H. (2011). 3D Simulations of M 7 Earthquakes on the Wasatch fault, Utah, Part I: Long-period (0–1 Hz) ground motions. *Journal Geophysical Research*, 101(5), 2045–2063.
- Roten, D., Olsen, K., Day, S., Cui, Y., & Fäh, D. (2014). Expected seismic shaking in Los Angeles reduced by San Andreas fault zone plasticity. *Journal Geophysical Research*, 41(8), 2769–2777.
- Shi, Z., & Day, S. M. (2013). Rupture dynamics and ground motion from 3-D rough-fault simulations. *Journal Geophysical Research*, 118(3), 1122–1141.
- Templeton, E., Bhat, H., Dmowska, R., & Rice, J. (2010). Dynamic rupture through a branched fault configuration at Yucca Mountain, and resulting ground motions. *Journal Geophysical Research*, 100(4), 1485–1497.
- Vidale, J. E., & Li, Y.-G. (2003). Damage to the shallow Landers fault from the nearby Hector Mine earthquake. *Nature*, 421(6922), 524–526.
- Wyllie, D., & Mah, C. (2004). *Rock slope engineering*. Boca Raton: CRC Press.

(Received July 31, 2016, revised December 21, 2016, accepted January 2, 2017, Published online February 3, 2017)